

BARYONIFICATION III: AN ACCURATE ANALYTICAL MODEL FOR THE DISPERSION MEASURE PROBABILITY DENSITY FUNCTION OF FAST RADIO BURSTS

MOHAMMADREZA TORKAMANI[†], ROBERT REISCHKE^{*}

Argelander-Institut für Astronomie, Universität Bonn, Auf dem Hügel 71, D-53121 Bonn, Germany

MICHAEL KOVAC

Jodrell Bank Centre for Astrophysics, Department of Physics and Astronomy, The University of Manchester, Manchester M13 9PL, United Kingdom
 Argelander-Institut für Astronomie, Universität Bonn, Auf dem Hügel 71, D-53121 Bonn, Germany

ANDRINA NICOLA

Jodrell Bank Centre for Astrophysics, Department of Physics and Astronomy, The University of Manchester, Manchester M13 9PL, United Kingdom

JOZEF BUCKO, ALEXANDRE REFREGIER

Institute for Particle Physics and Astrophysics, ETH Zurich, Wolfgang Pauli Strasse 27, 8093 Zurich, Switzerland

SAMBIT K. GIRI

Department of Astronomy and Oskar Klein Centre, AlbaNova, Stockholm University, SE-10691 Stockholm, Sweden

AUREL SCHNEIDER

Department of Astrophysics, University of Zurich, Winterthurerstrasse 190, 8057 Zurich, Switzerland

STEFFEN HAGSTOTZ

Universitäts-Sternwarte, Fakultät für Physik, Ludwig-Maximilians Universität München, Scheinerstraße 1, D-81679 München, Germany and
 Excellence Cluster ORIGINS, Boltzmannstraße 2, D-85748 Garching, Germany

Version January 27, 2026

ABSTRACT

We develop a fully analytical framework for predicting the one-point probability distribution function (PDF) of dispersion measures (DM) for fast radio bursts (FRBs) using the baryonification (BFC) model. BFC provides a computationally efficient alternative to expensive hydrodynamical simulations for modelling baryonic effects on cosmological scales. By applying the halo mass function and halo bias, we convolve contributions from individual halos across a range of masses and redshifts to derive the large-scale structure contribution to the DM PDF. We validate our analytical predictions against consistency-check simulations and compare them with the IllustrisTNG hydrodynamical simulation across a range of redshifts up to $z = 5$, demonstrating excellent agreement. We demonstrate that our model produces consistent results when fitting gas profiles and predicting the PDF, and vice versa. We show that the BFC parameters controlling the gas profile, particularly the halo mass scale (M_c), mass-dependent slope (μ), and outer truncation (δ), are the primary drivers of the PDF shape. Additionally, we investigate the validity of the log-normal approximation commonly used for DM distributions, finding that it provides a sufficient description for a few hundred FRBs. Our work provides a self-consistent model that links gas density profiles to integrated DM statistics, enabling future constraints on baryonic feedback processes from FRB observations.

Keywords: Cosmology, Fast Radio Bursts, Circumgalactic Medium, Baryonic Feedback

1. INTRODUCTION

Fast radio bursts (FRBs) are brief yet extremely bright transients, lasting only a few milliseconds and spanning frequencies from roughly 100 MHz to several GHz. As the initial pulse travels through the ionised gas in both the galactic and

intergalactic medium (IGM), it becomes dispersed: lower-frequency (ν) components arrive later, producing a delay that scales as $\Delta t(\nu) \propto \Delta(1/\nu^2)$. The proportionality constant, known as the dispersion measure (DM), corresponds to the total column density of free electrons along the line of sight (LOS) to the FRB (see e.g. Lorimer et al. 2007; Thornton et al. 2013; Petroff et al. 2015; Connor et al. 2016; Champion et al. 2016; Chatterjee et al. 2017).

[†]mohamadrezatorkamani@gmail.com

^{*}reischke@posteo.net, rreischke@astro.uni-bonn.de

Although the mechanism responsible for FRB radio emission remains uncertain, their isotropic sky distribution and typically large observed DMs strongly suggest that most events originate outside the Milky Way (though a subset may be Galactic; see e.g. [Andersen et al. 2020](#)). This extragalactic origin requires modelling the DM in a cosmological setting, but also enables FRBs to be a powerful cosmological probe. One refers to FRBs with an associated host as localised FRBs. The DM-redshift relation of those FRBs has been used to constrain the mean baryon density in the Universe ([Macquart et al. 2020](#)), the expansion rate ([Hagstotz et al. 2022](#); [James et al. 2022](#)), or fundamental physics such as the equivalence principle ([Reischke & Hagstotz 2023a](#)). A key aspect of these types of analyses is that they require the probability distribution function (PDF) of the DM. Early analyses of hydrodynamical cosmological simulations suggest that the DM induced by the electrons distributed in the large-scale structure (LSS) produce a PDF well described by a log-normal distribution ([Zhang et al. 2021](#); [Walker et al. 2024](#)). Given this simple functional form, the PDF can be fully specified by calculating the free-electron variance. It has therefore been realised that the uncertainty in the DM-redshift relation contains valuable information about the one-point statistical properties of the gas distribution (e.g. [McQuinn 2014](#); [Reischke & Hagstotz 2023b](#); [Medlock et al. 2024](#); [Sharma et al. 2025](#); [Medlock et al. 2025](#)). This is crucial as cosmological surveys such as Euclid ([Collaboration et al. 2025](#)) or Rubin Observatory Legacy Survey of Space and Time (LSST, [LSST Science Collaboration et al. 2009](#)) aspire to map the LSS deep into the non-linear regime by measuring the shapes and positions of billions of galaxies. The distribution of baryonic matter is influenced by feedback processes from Active Galactic Nuclei, Supernovae and others. In turn, these feedback mechanisms also influence the overall matter distribution in the Universe and, consequently, impact cosmological observables. It is on these non-linear scales that understanding the distribution of baryons has become paramount (e.g. [Chisari et al. 2019a](#), for an overview). [Reischke & Hagstotz \(2025\)](#); [Connor et al. \(2025\)](#) assumed a log-normal distribution for the DM-redshift relation and put constraints on baryonic feedback using $\sim 10^2$ FRBs.

Recently, [Konietzka et al. \(2025\)](#) remeasured the PDF in the IllustrisTNG simulation, finding considerable disagreements with previous results due to improved line-of-sight integration and interpolation. In particular, they found that the PDF is less well described by a log-normal distribution at low redshifts. A general question thus arises: how can the distribution of the multi-phase IGM be modelled efficiently? While conducting large suites of hydrodynamical simulations with cosmologically relevant volumes would be ideal for studying baryonic feedback, such calculations are computationally prohibitive in a cosmological analysis. As a result, several alternative methods have been developed to capture baryonic effects on the matter distribution, including halo-model-based approaches as well as emulating hydrodynamical simulations ([McCarthy et al. 2017](#); [Mead et al. 2020](#); [Tröster et al. 2022](#)). Alternatively, one can paint new haloes onto existing N -body simulations ([Osato & Nagai 2023](#)). A complementary approach is offered by the so-called baryonification method (first introduced in [Schneider & Teyssier 2015](#)), which relies on modifications to N -body simulations, using empirical functions to describe the gas, stellar, and dark matter profiles surrounding galaxy groups and clusters. The method can be calibrated against observations or hydrodynamical simulations, offering

a computationally efficient means of modelling cosmological probes. In recent years, several models and implementations based on baryonification have been developed (e.g. [Schneider et al. 2019](#); [Giri & Schneider 2021](#); [Aricò et al. 2021b](#); [Anbajagane et al. 2024](#)). Baryonification has been shown to reproduce the matter power spectra measured in hydrodynamical simulations across a range of feedback scenarios and observables: the suppression of the matter power spectrum ([Giri & Schneider 2021](#)), higher order statistics ([Aricò et al. 2021a](#); [Fluri et al. 2022](#); [Zürcher et al. 2023](#); [Lee et al. 2023](#); [Burger et al. 2025](#); [Zhou et al. 2025](#)), gas fractions ([Schneider et al. 2020](#); [Grandis et al. 2024](#)), or the kinematic Sunyaev-Zel'Dovich (kSZ) effect ([Schneider et al. 2022](#)). The most recent version was presented in [Schneider et al. \(2025\)](#) and is dubbed the baryonification (BFC) model. In [Kovač et al. \(2025\)](#) it was shown that BFC can consistently reproduce X-ray and kSZ observations.

In this work, we apply BFC to FRBs to link their observed DM to cosmological observables. An FRB signal propagates through three distinct environments before reaching the observer. It first travels through its host galaxy, then passes through the IGM, and finally traverses the Milky Way. Although [Reischke et al. \(2025\)](#) studied the host-galaxy contribution to the DM in detail, a comprehensive model for the IGM component is still lacking. Similar to the host galaxy, the statistical properties of the IGM's DM contribution depend strongly on baryonic feedback processes. We use the BFC model to develop a fully analytical model of the IGM contribution to the DM PDF of FRBs. In developing this model, we closely follow the approach of [Thiele et al. \(2019\)](#), who performed a similar calculation for the thermal Sunyaev–Zel'dovich effect. A related calculation of the DM one-point PDF was presented by [McQuinn \(2014\)](#); however, their analysis did not incorporate BFC and did not attempt accurate comparisons to hydrodynamical simulations. Combining the model presented in this paper with the host galaxy (which was tackled in [Reischke et al. \(2025\)](#)) and the Milky Way contributions (see e.g. [Yao et al. 2017](#); [Ocker & Cordes 2024](#)) will allow us to study FRBs consistently in a cosmological context.

This paper is organised as follows. In Section 2, we provide a brief introduction to the DM of FRBs, introduce the BFC model and describe the methods used in our calculations. In Section 3, we present the two simulations employed in this work, followed by Section 4, where we discuss our results. Finally, in Section 5, we conclude by summarising the main findings of this study. Throughout this paper, we define the virial radius (r_{200}) as the radius within which the mean density is 200 times the critical density of the Universe. The corresponding virial mass (M_{200}) is the total mass enclosed within this virial radius. To maintain consistency with the IllustrisTNG simulation, we adopt the Planck 2015 cosmological parameters ([Planck Collaboration et al. 2016](#)): baryon density $\Omega_b = 0.0486$, matter density $\Omega_m = 0.3089$, scalar spectral index $n_s = 0.9667$, root-mean-square fluctuation amplitude $\sigma_8 = 0.8159$, and the dimensionless Hubble constant $h = 0.6774$.

2. METHODOLOGY

In this section, we first introduce the basic properties of FRBs and their associated DM in Section 2.1. In Section 2.2, we introduce BFC and all relevant profiles used. We calculate the one-point PDF of the DM of the LSS in Section 2.3. In Section 2.4, we compare our approach to other works. Lastly, in Section 2.5, we describe an emulator used to speed up analytical calculations. All cosmological quantities are calcu-

Parameter	Lower limit	Upper limit	Fiducial	Eq.	Description
Varied	η	0	0.5	0.017	15
	$d\eta$	0	0.5	0.229	18
	N_{star}	0	0.05	0.0074	15
	c_{iga}	0	1	0.0093	17
	θ_{co}	0	0.5	0.231	12
	$\log_{10} M_{\text{c}}$	11	15	12.86	13
	μ	0	2	0.721	13
Fixed	δ	4	8	5.47	12
	α		1		12
	γ		1.5		12
	M_{star}		$2.5 \times 10^{11} h^{-1} M_{\odot}$		15
	ζ		1.376		15
					Low-mass slope of the central galaxy profile

Table 1: All BFC parameters and their respective flat prior limits, as well as the fiducial values obtained from fitting the gas profiles of Illustris TNG directly (compare Figure 6). If only a single number for the upper and lower limits is given, the parameter is fixed. The last column gives a brief physical interpretation of the parameter and a reference to the equation in which it first occurs.

lated using the Core Cosmology Library (CCL [Chisari et al. 2019b](#)). Linear matter power spectra are computed with CAMB ([Lewis et al. 2000](#)). Furthermore, we use some functionality of astropy ([Astropy Collaboration et al. 2022](#)).

2.1. Dispersion Measure of Fast Radio Bursts

One of the key characteristics of FRBs is their DM. As a radio signal from an FRB at direction \mathbf{n} and redshift z travels through the ionised gas between the source and the observer, each frequency travels at a different effective speed, leading to delays quantified by the following relation

$$\Delta t \propto \Delta(1/\nu^2). \quad (1)$$

The proportionality constant is the DM and is given by the integral of the comoving electron density n_{e} along the LOS:

$$\text{DM}(z, \mathbf{n}) = \int_0^z n_{\text{e}}(z', \mathbf{n})(1+z') \frac{cdz'}{H(z')}, \quad (2)$$

where c is the speed of light and $H(z)$ is the Hubble function.

It is convenient to split the DM into different contributions:

$$\text{DM}_{\text{total}}(z, \mathbf{n}) = \text{DM}_{\text{MW}}(\mathbf{n}) + \text{DM}_{\text{LSS}}(z, \mathbf{n}) + \text{DM}_{\text{host}}(z), \quad (3)$$

where DM_{MW} , DM_{LSS} , and DM_{host} are the DMs of the Milky Way, the LSS, and the host galaxy, respectively. The redshift z and positional, \mathbf{n} , dependencies are written out explicitly for all components. The Milky Way component does not vary with redshift, and the host term is unaffected by the host galaxy's spatial location. The former can be measured from galactic Pulsar dispersion measures (e.g. [Ocker et al. 2020](#)) and has been modelled in ([Ocker & Cordes 2024](#)) using a simplified model introduced in [Cordes & Lazio \(2002\)](#). Another work ([Yao et al. 2017](#)) introduced a different model for the interstellar medium contribution of the Milky Way; most cosmological results, however, do not depend on this specific choice as long as the galactic disk is avoided (see e.g. [Reischke & Hagstotz 2023a](#)). DM_{host} was modelled in [Reischke et al. \(2025\)](#) using the BFC model and was shown to match the output of hydrodynamical simulations ([Theis et al. 2024; Medlock et al. 2024](#)). Here, we will put forward an equivalent model for DM_{LSS} based on the same BFC model.

2.2. Baryonification Model

BFC was proposed and subsequently improved in a series of papers, see e.g. [Schneider & Teyssier \(2015\)](#); [Schneider et al. \(2025\)](#) for the initial proposal and the latest implementation. The goal is to model baryonic effects by displacing particles in dark matter-only (DMO) simulations. Since DMO simulations are less complex and computationally intensive than hydrodynamical simulations, BFC offers a faster, more efficient approach to studying the baryon distribution. Crucially, BFC is also more interpretable due to a set of flexible, physically motivated parameters that allow it to describe vastly different feedback scenarios. Table 1 summarises those parameters.

BFC displaces dark matter and baryonic particles differently; in this work, we focus on the baryonic component. For the baryonic component in BFC, the initial density profile is taken directly from the DMO simulation. It is described as the sum of a truncated NFW profile ([Navarro et al. 1997](#); [Baltz et al. 2009](#)) and a two-halo term:

$$\rho_{\text{bar},i}(r) = f_{\text{bar}} [\rho_{\text{NFW}}(r) + \rho_{2h}(r)], \quad (4)$$

where $f_{\text{bar}} = \Omega_b/\Omega_m$ is the cosmic baryon fraction. The two-halo term is defined as:

$$\rho_{2h}(r) = [1 + b(\nu)\xi_{\text{lin}}(r)] \Omega_b \rho_{\text{crit}}, \quad (5)$$

with $b(\nu)$ the halo bias (specifically we use the one presented in [Tinker et al. 2008](#)) and $\xi_{\text{lin}}(r)$ the linear matter correlation function.

To obtain the final baryonic density profile, the initial NFW component is replaced by the sum of a gas density profile and a stellar density profile:

$$\rho_{\text{bar},f}(r) = \rho_{\text{gas}}(r) + \rho_{\text{star}}(r) + f_{\text{bar}} \rho_{2h}(r). \quad (6)$$

Each of these profiles has its own analytical form and depends on a distinct set of BFC parameters, which must be constrained using observational data.

The enclosed mass of each component can be obtained by integrating the density profile.

$$M_{\chi}(R) = 4\pi \int_0^R r^2 \rho_{\chi} dr = f_{\chi} Y_{\chi}(R), \quad (7)$$

where f_{χ} is the abundance of components χ and Y_{χ} is nor-

malised such that

$$Y_\chi(\infty) = M_{\text{tot}}. \quad (8)$$

Given this, the total mass of each species is purely determined by its abundance (f_χ).

We then introduce a displacement function, $d(r)$, which maps particle positions in the DMO simulation to those that reproduce the desired baryonic density profile. The mapping is defined through the inverted cumulative mass profile:

$$r_{\text{bar}} = \text{inv}[M_{\text{bar}}(r)] \quad (9)$$

$$d(r) = r_{\text{bar,f}} - r_{\text{bar,i}}, \quad (10)$$

where $\text{inv}[M_{\text{bar}}(r)]$ denotes the inverse of the cumulative mass profile. This allows us to displace particles in DMO simulations by

$$r_{\text{bar,f}} = r_{\text{bar,i}} + d(r), \quad (11)$$

in order to obtain the baryon density profile from the DMO profile.

The gas profile in the BFC model consists of two components: a hot gas component (HGA) and a cold gas component (IGA). We assume that the HGA is fully ionised, while the IGA is mostly neutral and therefore does not directly affect our results. Consequently, our discussion will focus on the HGA. The analytic form of the hot gas density profile is modelled as a cored double power law:

$$\rho_{\text{hga}}(r) \propto \frac{f_{\text{bar}} - f_{\text{star}}(M_{200}) - f_{\text{iga}}(M_{200})}{\left[1 + \left(\frac{r}{r_c}\right)^\alpha\right]^{\beta/\alpha} \left[1 + \left(\frac{r}{r_t}\right)^\gamma\right]^{\delta/\gamma}}, \quad (12)$$

where M_{200} is the halo mass, $r_c = \theta_c r_{200}$ denotes the core radius, and $r_t = \epsilon r_{200}$ specifies the truncation radius. Throughout this work, the truncation exponent is fixed to $\gamma = 3/2$.

The slope β of the gas profile varies with halo mass. When accounting for AGN feedback, lower-mass haloes typically exhibit shallower gas density profiles, i.e. lower β . This behaviour is captured by the following parametrisation:

$$\beta(M_{200}) = \frac{3(M_{200}/M_c)^\mu}{1 + (M_{200}/M_c)^\mu}. \quad (13)$$

The stellar profile is assumed to follow the dark matter distribution:

$$\rho_{\text{sga}}(r) = \frac{f_{\text{sga}}}{4\pi r^2} \frac{d}{dr} M_{\text{nfw}}(\xi r), \quad (14)$$

where back-reaction was included. Note that there is a separate profile for the central galaxy. We parametrise the stellar mass fraction as:

$$f_{\text{star}}(M_{200}) = \frac{N_{\text{star}}}{\left(\frac{M_{200}}{M_{\text{star}}}\right)^{-\zeta} + \left(\frac{M_{200}}{M_{\text{star}}}\right)^\eta}. \quad (15)$$

Lastly, the cold gas profile is

$$\rho_{\text{iga}}(r) = \frac{\rho_{\text{iga},0}}{r^3} \exp(-r/r_{200}), \quad (16)$$

with the corresponding fraction defined as

$$f_{\text{iga}}(M_{200}) = c_{\text{iga}} f_{\text{cga}}(M_{200}), \quad (17)$$

with $f_{\text{cga}}(M)$ given by

$$f_{\text{cga}}(M_{200}) = \frac{N_{\text{star}}}{\left(\frac{M_{200}}{M_{\text{star}}}\right)^{-\zeta} + \left(\frac{M_{200}}{M_{\text{star}}}\right)^{\eta+d\eta}}, \quad (18)$$

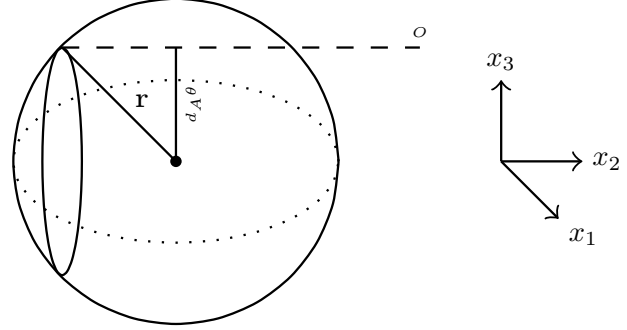


Figure 1. : Geometry of the projected DM as illustrated in Equation (19). Here d_A is the angular diameter distance at the redshift of the halo. The projection is carried out along the x_2 -axis towards the observer O .

where $\zeta = 1.376$ and $M_{\text{star}} = 2.5 \times 10^{11} h^{-1} M_\odot$. All parameters, except for ϵ , which depends on the choice of the NFW profile, are free parameters and influence the shape of the profile. We will examine the impact of these parameters on the final PDF later. Table 1 summarises the parameters used here, together with a quick reference for each parameter to its respective occurrence in the model.

2.3. DM one-point PDF of LSS

In this section, we explain how to calculate the one-point PDF for the LSS. First, we will start with the DM profile of a single halo and then closely follow the methodology of Thiele et al. (2019), who performed a similar calculation for the thermal Sunyaev-Zel'dovich effect. For completeness, we rederive all relevant expressions presented in Thiele et al. (2019). Throughout this section, for a more concise notation, we denote all halo masses by M rather than M_{200} .

Reischke et al. (2025) presented an analytical model for the DM of FRBs within their host halos based on BFC. Here, the situation is slightly different. The geometry is shown in Figure 1. We want to know the contribution to the DM of a halo of mass M and at redshift z which has been traversed by an FRB at angle θ from the centre. Suppose $\text{DM}_{M,z}^{(3)}(x_1, x_2, x_3)$ is the DM of an FRB at position $\mathbf{r}^T = (x_1, x_2, x_3)$ relative to the halo centre, where we project along the x_3 axis without loss of generality due to spherical symmetry. Due to the latter, the DM profile depends only on the radial distance from its centre. We can write the two-dimensional DM profile, $\text{DM}(M, z, \theta)$, of the isolated halo under consideration as:

$$\text{DM}(M, z, \theta) = \text{DM}_{M,z}^{(3)}(0, -\sqrt{r^2 - (d_A \theta)^2}, d_A \theta), \quad (19)$$

where $d_A = d_A(z)$ is the comoving angular diameter distance to the halo centre, θ is the angular separation on the sky, $\text{DM}_{M,z}^{(3)}$ is the three-dimensional DM profile within the halo, and r is the halo radius. The DM of such a halo can also be written as:

$$\text{DM}(M, z, \theta) = (1+z)^2 \int dx_2 \frac{\rho_{\text{hga}}[r(x_2, \theta, z), M, z]}{\mu_e m_p}, \quad (20)$$

with the proton mass m_p and the mean molecular weight per electron $\mu_e = 1.17$. Note that the quantities here are all comoving.

To calculate the one-point PDF of the FRB DMs, we proceed as follows: We first consider a small volume element and a mass bin in which halo overlap can be neglected. Then, we

compute the PDF within this region and afterwards convolve all halo mass bins along the LOS to account for overlapping halos. Finally, to incorporate halo clustering, we compute the one-point PDF for a fixed linear field $\delta_{\text{lin}}(\mathbf{n}, z)$ and average over Gaussian realisations of the field δ_{lin} . As per usual, it is advantageous to work in Fourier space due to the convolution theorem. Throughout, we will use the following Fourier convention, so that the Fourier transform of the one-point PDF is:

$$\tilde{P}(\lambda) = \int dDM P(DM) e^{i\lambda DM}. \quad (21)$$

$\tilde{P}(\lambda)$ can then be written as

$$\tilde{P}(\lambda) = \langle \exp [i\lambda DM(\mathbf{n})] \rangle, \quad (22)$$

where $DM(\mathbf{n})$ is the DM at a fixed sight-line \mathbf{n} . This is simply the characteristic function of the random variable DM . The expectation value in Equation (22) can be calculated by averaging over random halo placements. The number of halos in the volume element dV with masses between M and $M+dM$ is given by

$$dN = \frac{dn(M, z)}{dM} dV dM, \quad (23)$$

where $dn(M, z)/dM$ is the halo mass function. The angular halo number density in these narrow bins is

$$\frac{dn}{d\Omega} = \frac{\chi^2(z)}{H(z)} \frac{dn(M, z)}{dM} dM dz, \quad (24)$$

where $\chi(z)$ is the comoving distance to redshift z . If we choose dz and dM to be sufficiently small, then overlaps between halos can be neglected. For numerical purposes, we assume that each halo has a finite angular radius θ_{max} , beyond which its contribution to the DM can be neglected. Typically, we use θ_{max} to be three times the virial radius. Contributions beyond that will be dominated entirely by the two-halo term and will not change the shape of the PDF but only its mean.

With the assumptions discussed previously, Equation (22) can be replaced with an integral over the angular DM function as described in Equation (19), i.e.

$$\tilde{P}(\lambda) = \left(1 - \frac{dn}{d\Omega} \pi \theta_{\text{max}}^2\right) + \frac{dn}{d\Omega} \int_0^{\theta_{\text{max}}} d\theta 2\pi \theta e^{i\lambda DM(\theta)}. \quad (25)$$

The first term represents the probability that no halo overlaps with the sight-line \mathbf{n} , while the second term integrates over the overlapping locations.

Equation (25) can be rewritten in the following compact form

$$\tilde{P}(\lambda) = 1 + \frac{\chi^2(z)}{H(z)} \frac{dn(M, z)}{dM} \tilde{Y}(M, z, \lambda) dM dz, \quad (26)$$

where

$$\tilde{Y}(M, z, \lambda) = \int d\theta 2\pi \theta \left(e^{i\lambda DM(M, z, \theta)} - 1 \right). \quad (27)$$

At this point, we can calculate the one-point PDF considering all masses and redshifts. For now, we assume that we can neglect halo clustering; thus, the contribution to the DM from each halo bin is independent. For N bins $(M_1, z_1) \cdots (M_N, z_N)$, the complete PDF can be calculated by convolution.

For a differential bin $(dM dz)$ Equation (26) is equivalent to

$$\tilde{P}(\lambda) = \exp \left(\frac{\chi^2(z)}{H(z)} \frac{dn(M, z)}{dM} \tilde{Y}(M, z, \lambda) dM dz \right). \quad (28)$$

Since the convolution becomes multiplication in Fourier space, we will have:

$$\begin{aligned} \tilde{P}(\lambda) &= \lim_{N \rightarrow \infty} \prod_{i=1}^N \tilde{P}_{M_i, z_i}(\lambda) \\ &= \exp \int \frac{\chi^2(z)}{H(z)} \frac{dn(M, z)}{dM} \tilde{Y}(M, z, \lambda) dM dz. \end{aligned} \quad (29)$$

Equation (29) is the final result for the one-point PDF of the DM in Fourier space, neglecting halo clustering. Note that the PDF derived in this way does not capture the mean contribution to the DM, as we would have to include the two-halo term up to $r \rightarrow \infty$, which is numerically difficult as it provides a constant term to the Fourier transform. We discuss this in more detail in Section 4.1. The model, however, stays fully predictive as the mean (see Equation 51) can be computed directly from the cosmological parameters.

We now incorporate halo clustering into the PDF. We denote the unclustered PDF (Equation 29) and clustered PDF by $\tilde{P}_u(\lambda)$ and $\tilde{P}_{\text{cl}}(\lambda)$, respectively. The derivation involves two main steps. First, we calculate the one-point PDF $\tilde{P}_\delta(\lambda, \mathbf{n})$ for a fixed realisation of the linear density field $\delta_{\text{lin}}(\mathbf{n}, z)$. Next, we average over all realisations of the Gaussian field δ_{lin} to obtain $\tilde{P}_{\text{cl}}(\lambda)$. (Note that \tilde{P}_δ depends on \mathbf{n} because a specific realisation of δ_{lin} breaks translational invariance, while $\tilde{P}_{\text{cl}}(\lambda)$ remains translationally invariant, as expected.)

$\tilde{P}_\delta(\lambda, \mathbf{n})$ can be calculated by biasing the halo mass function with the halo bias $b(M, z)$ in Equation (29). This corresponds to a peak–background split: the large-scale linear density field provides a background that modulates the local number of halos, which is captured by the biasing with δ_{lin} :

$$\begin{aligned} \tilde{P}_\delta(\lambda, \mathbf{n}) &= \exp \int dM dz \frac{\chi^2(z)}{H(z)} \tilde{Y}(M, z, \lambda) \\ &\quad \left\{ \frac{dn(M, z)}{dM} [1 + b(M, z) \delta_{\text{lin}}(\mathbf{n}, z)] \right\}. \end{aligned} \quad (30)$$

This expression assumes that the linear density field varies only on scales much larger than the typical size of a halo, such that one can define a sufficiently large region around \mathbf{n} over which $\delta_{\text{lin}}(\mathbf{n} + \mathbf{n}', z) \simeq \delta_{\text{lin}}(\mathbf{n}, z)$. In this regime, the long-wavelength linear density field acts as a locally constant background that modulates the mean halo abundance.

Now we need to average over realisations of the linear density field in Equation (30):

$$\tilde{P}_{\text{cl}}(\lambda) = \langle \tilde{P}_\delta(\lambda, \mathbf{n}) \rangle_{\delta(\mathbf{n}, z)}. \quad (31)$$

By defining two auxiliary functions

$$A(\lambda, \mathbf{n}) \equiv \int dz \delta_{\text{lin}}(\mathbf{n}, z) \alpha(z, \lambda), \quad (32)$$

$$\alpha(z, \lambda) \equiv \int dM b(M, z) \frac{\chi^2(z)}{H(z)} \frac{dn(M, z)}{dM} \tilde{Y}(M, z, \lambda), \quad (33)$$

Equation (30) can be written as:

$$\tilde{P}_\delta(\lambda, \mathbf{n}) = \tilde{P}_u(\lambda) e^{A(\lambda, \mathbf{n})}. \quad (34)$$

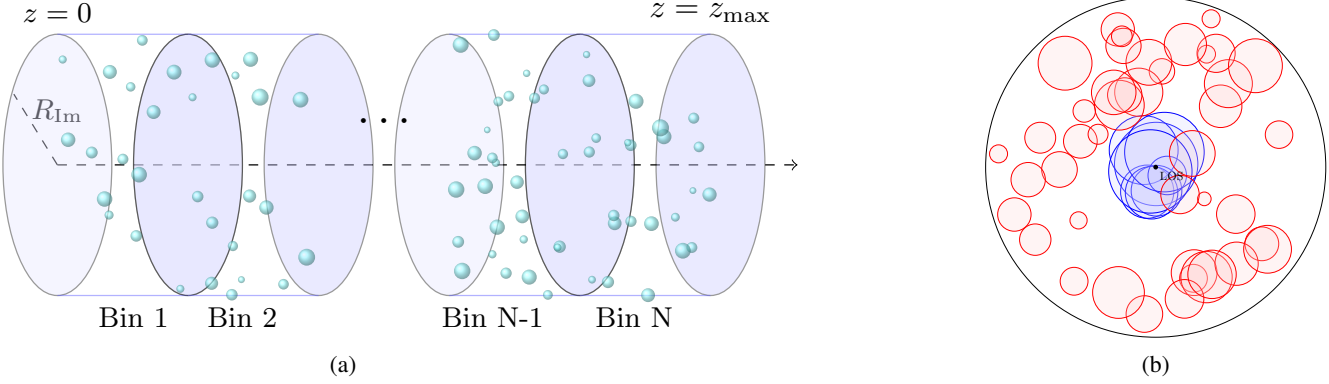


Figure 2.: Figure (a) illustrates an example of the simulation setup, where the volume is divided into equally spaced redshift bins. Figure (b) displays the halos projected onto a plane for an arbitrary bin. Halos that intersect with the LOS are shown in light blue, and only their contributions are included in the analysis. This serves as a consistency-check simulation, as it must reproduce, by definition, the analytical treatment of the unclustered case Equation (29).

By using the identity $\langle e^x \rangle = e^{\frac{1}{2}\langle x^2 \rangle}$ for a Gaussian random variable x , Equation (31) can be rewritten as:

$$\tilde{P}_{\text{cl}}(\lambda) = \tilde{P}_{\text{u}}(\lambda) \exp \frac{1}{2} \langle A^2(\lambda, \mathbf{n}) \rangle_{\delta}. \quad (35)$$

The quantity $\langle A^2 \rangle$ can be calculated using linear perturbation theory. In this regime, the density contrast factorises into a time-dependent growth factor normalised to one at redshift zero and a purely spatial field,

$$\delta_{\text{lin}}(\mathbf{x}, z) = D(z) \delta_{\text{lin}}(\mathbf{x}). \quad (36)$$

Along the LOS, where $\mathbf{x} = \chi(z) \mathbf{n}$, this relation becomes

$$\delta_{\text{lin}}(\mathbf{n}, z) = D(z) \delta_{\text{lin}}(\chi(z) \mathbf{n}). \quad (37)$$

Then one can calculate $\langle A^2(\lambda, \mathbf{n}) \rangle_{\delta}$ as follows:

$$\begin{aligned} \langle A^2(\lambda, \mathbf{n}) \rangle_{\delta} &= \int dz dz' D(z) D(z') \alpha(z, \lambda) \alpha(z', \lambda) \\ &\quad \langle \delta_{\text{lin}}(\chi(z) \mathbf{n}) \delta_{\text{lin}}(\chi(z') \mathbf{n}) \rangle. \end{aligned} \quad (38)$$

We now evaluate the two-point correlator by expressing the density field in Fourier space:

$$\begin{aligned} &\langle \delta_{\text{lin}}(\chi(z) \mathbf{n}) \delta_{\text{lin}}(\chi(z') \mathbf{n}) \rangle \\ &= \int \frac{d^3 k}{(2\pi)^3} \frac{d^3 k'}{(2\pi)^3} \langle \delta_{\text{lin}}(\mathbf{k}) \delta_{\text{lin}}(\mathbf{k}') \rangle e^{i[\chi(z)\mathbf{k} + \chi(z')\mathbf{k}'] \cdot \mathbf{n}}, \end{aligned} \quad (39)$$

by definition, $\langle \delta_{\text{lin}}(\mathbf{k}) \delta_{\text{lin}}(\mathbf{k}') \rangle = (2\pi)^3 \delta_D(\mathbf{k} + \mathbf{k}') P_{\text{lin}}(k)$, where $P_{\text{lin}}(k)$ denotes the linear matter power spectrum. Using this relation and performing the integral over \mathbf{k}' , Equation (39) can be rewritten as

$$\begin{aligned} &\langle \delta_{\text{lin}}(\mathbf{n}) \delta_{\text{lin}}(\mathbf{n}) \rangle \\ &= \int \frac{d^3 k}{(2\pi)^3} \frac{d^3 k'}{(2\pi)^3} (2\pi)^3 \delta_D(\mathbf{k} + \mathbf{k}') P_{\text{lin}}(k) e^{i[\chi(z)\mathbf{k} + \chi(z')\mathbf{k}'] \cdot \mathbf{n}} \\ &= \int \frac{d^3 k}{(2\pi)^3} P_{\text{lin}}(k) e^{i[\chi(z) - \chi(z')] \mathbf{k} \cdot \mathbf{n}}. \end{aligned} \quad (40)$$

At this stage, we decompose the wavevector \mathbf{k} into components parallel and perpendicular to the LOS, denoted by k_{\parallel} and \mathbf{k}_{\perp} , respectively. Applying the Limber approximation,

$$P_{\text{lin}}\left(\sqrt{k_{\perp}^2 + k_{\parallel}^2}\right) \simeq P_{\text{lin}}(k_{\perp}), \quad (41)$$

Equation (40) can then be written as

$$\begin{aligned} &\int \frac{d^3 k}{(2\pi)^3} P_{\text{lin}}(k) e^{i[\chi(z) - \chi(z')] \mathbf{k} \cdot \mathbf{n}} \\ &= \int \frac{d^2 k_{\perp}}{(2\pi)^2} P_{\text{lin}}(k_{\perp}) \int \frac{dk_{\parallel}}{2\pi} e^{i[\chi(z) - \chi(z')] k_{\parallel}} \\ &= \int \frac{d^2 k_{\perp}}{(2\pi)^2} P_{\text{lin}}(k_{\perp}) \delta_D[\chi(z) - \chi(z')]. \end{aligned} \quad (42)$$

Substituting Equation (42) into Equation (38) and using the identity

$$\delta_D[\chi(z) - \chi(z')] = H(z) \delta_D(z - z'), \quad (43)$$

we obtain

$$\langle A^2(\lambda, \mathbf{n}) \rangle_{\delta} = \int dz H(z) D^2(z) \alpha^2(z, \lambda) \int \frac{dk}{2\pi} P_{\text{lin}}(k). \quad (44)$$

With all the previous calculations, the final expression for the one-point PDF in Fourier space is given by:

$$\begin{aligned} \tilde{P}_{\text{cl}}(\lambda) &= \tilde{P}_{\text{u}}(\lambda) \exp \left(\frac{1}{2} \int dz H(z) D^2(z) \alpha^2(z, \lambda) \right. \\ &\quad \left. \times \int \frac{dk}{2\pi} P_{\text{lin}}(k) \right). \end{aligned} \quad (45)$$

Unless stated otherwise, we will always use this version of the PDF and not the unclustered one. However, the overall effect of clustering on the DM PDF is small.

2.4. Comparison to other works

As discussed before, McQuinn (2014) presented an analysis very similar to ours. In the following, we show that the two approaches are equivalent.

The expression for the PDF of the LSS contribution to the FRB DM derived in McQuinn (2014) is given by:

$$\tilde{P}(\lambda | z_s) = \exp \left[\int_0^{\chi(z_s)} d\chi \left(A + \frac{B^2 \Delta \chi \sigma_{\Delta \chi}^2}{2} \right) \right], \quad (46)$$

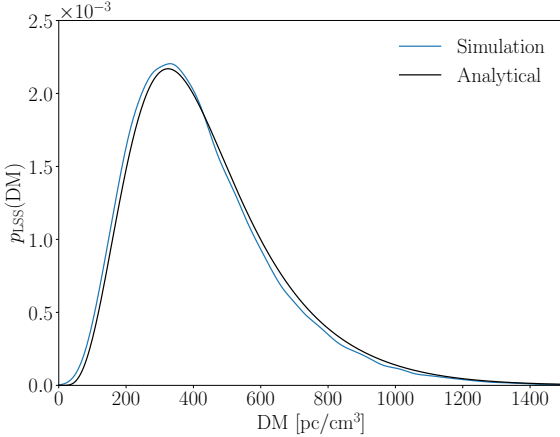


Figure 3. : Comparison between the DM PDF obtained from simulations (blue) and the analytical result (black) at redshift $z = 1.5$. Both methods use the same BFC parameters and account only for the electron density fluctuations δ_e , excluding the mean contribution. The shaded region represent the 3σ confidence interval calculated using the covariance matrix.

where

$$A = \int dM d^2R a^{-2} \frac{dn(M, z)}{dM} \left(e^{-i\lambda\Delta_{DM}(R, M)} - 1 \right), \quad (47)$$

$$B = \int dM d^2R a^{-2} \frac{dn(M, z)}{dM} b(M, z) \times \left(e^{-i\lambda\Delta_{DM}(R, M)} - 1 \right), \quad (48)$$

$$\sigma_{\Delta\chi}^2 = \int \frac{d^2k_{\perp} dk_{\parallel}}{(2\pi)^3} P_{\delta}(k) \text{sinc}^2 \left(\frac{\Delta\chi k_{\parallel}}{2} \right). \quad (49)$$

Here, a denotes the scale factor, R is the proper impact parameter, and $\Delta_{DM}(R, M)$ represents the DM profile as a function of radius.

The first term in Equation (46) is equivalent to Equation (29). Noting that $dz/H(z) = d\chi$, the factor a^{-2} arises from converting the proper impact parameter to the comoving one, and the area element d^2R corresponds to $\chi^2 (2\pi\theta d\theta)$.

In the second term, the only difference is that we carry out the line-of-sight integral of the matter power spectrum directly, whereas McQuinn (2014) assumes a plane-parallel approximation. Overall, Equation (46) is equivalent to Equation (45).

2.5. Emulator

The pipeline for computing the analytical result presented in Equation (45) is computationally expensive. To reduce computation time, we train a machine learning model to emulate the output, enabling rapid evaluations without recalculating the full expression for each parameter set. For this purpose, we use **CosmoPower**, a library designed explicitly for machine-learning-accelerated Bayesian inference (for more details, see Spurio Mancini et al. 2022).

Although **CosmoPower** was initially designed for cosmological power spectrum emulation, its methods are general and applicable to a wide range of scientific problems. In our work, we use **CosmoPower** to train a model that emulates the PDF. For more details, we refer the reader to Appendix A.

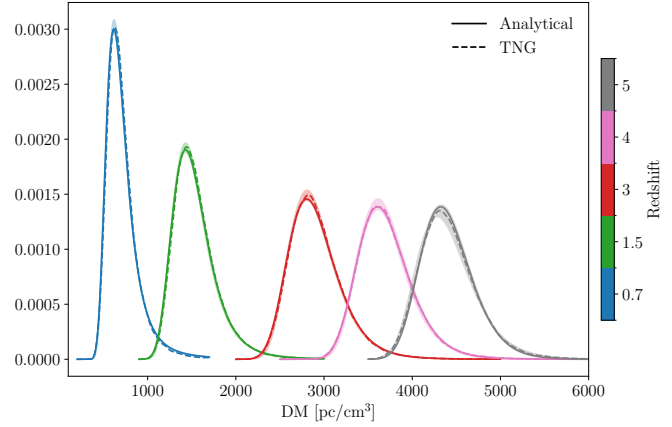


Figure 4. : Comparison of the analytical PDF for the DM of FRBs with results from the TNG simulation across various redshifts. The solid lines represent the analytical predictions, while the shaded regions indicate the 68% confidence intervals. The dashed lines show the corresponding results from the TNG simulation.

3. SIMULATION AND COVARIANCE

In this section, we discuss two types of simulations, of varying complexity, which we employ to evaluate the performance of our analytical model. First, we present a simple consistency-check simulation assuming only random halo placements and analytical profiles. Those simulations are also used to estimate the covariance of the DM PDF. Second, we use the results from the IllustrisTNG hydrodynamical simulation to demonstrate that our model accurately predicts the DM PDF.

3.1. Consistency-check simulation

To validate our analytical results, we perform a Poisson simulation to obtain the DM PDF at various redshifts. We start by dividing a cylindrically-shaped comoving volume into tomographic redshift bins. Halos are then randomly distributed within each bin according to the halo mass function, and subsequently projected onto a plane (see Figure 2 for a sketch). We compute the DM by evaluating the contribution from halos intersecting the LOS. This provides a single DM value. By repeating this procedure for different sightlines, we can generate a histogram of the DM values, which serves as an estimate of the PDF. This corresponds to a single realisation of the consistency-check simulation.

3.2. Covariance estimation

By running multiple realisations of the Poisson simulation, we estimate the covariance of the resulting PDFs as the sample covariance with components:

$$\mathbf{C}_{ij} = \frac{1}{n-1} \sum_{k=1}^n (X_i^{(k)} - \bar{X}_i)(X_j^{(k)} - \bar{X}_j), \quad (50)$$

where n is the number of simulation realisations, $X_i^{(k)}$ is the value of the PDF in bin i from the k -th realisation and \bar{X}_i is the mean value of the PDF in bin i across all simulations. Theoretically, this covariance has two contributions: one induced from the LSS directly, i.e. cosmic variance, and a second one from the finite amount of sightlines available, i.e. the number

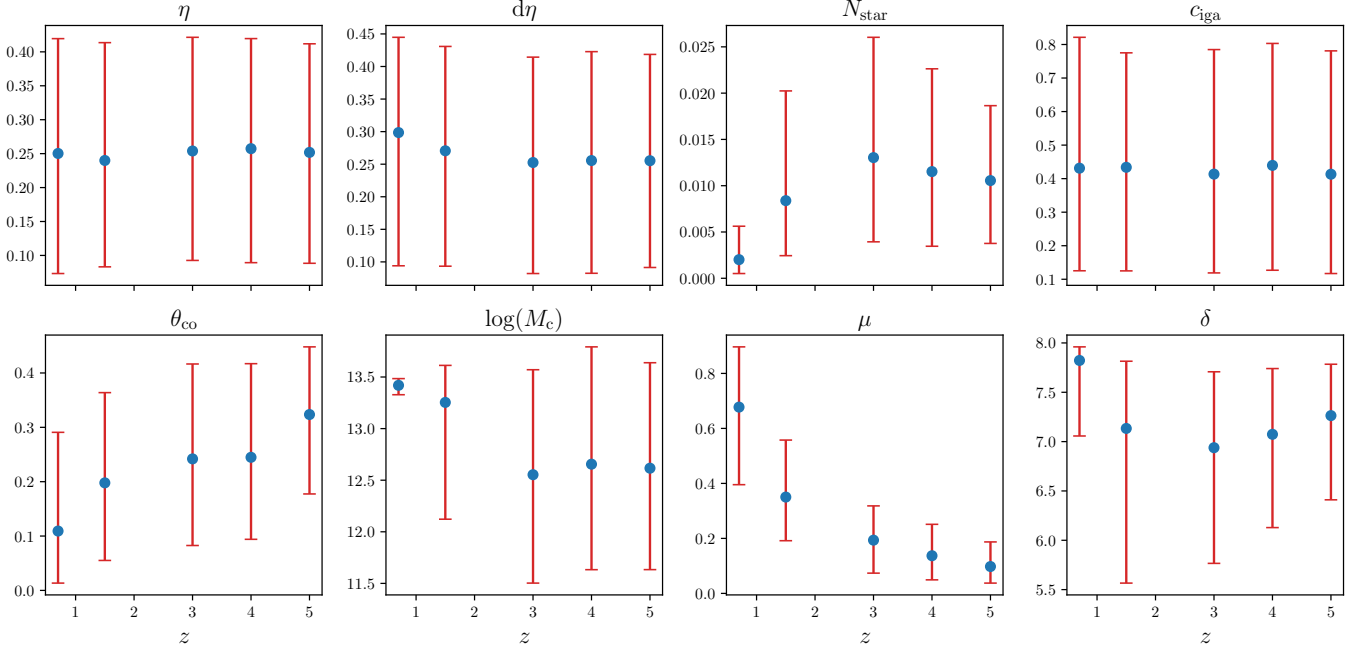


Figure 5.: Model parameters obtained from fitting to the IllustrisTNG simulation as a function of redshift for $\sim 10^4$ FRBs. Red error bars indicate the 68% confidence intervals, and blue points mark the highest posterior probabilities.

of FRBs. If the number of sightlines sampled tends to infinity, this corresponds to the cosmic-variance-induced covariance of the PDF.

3.3. IllustrisTNG

The IllustrisTNG simulation suite (Nelson et al. 2019; Pillepich et al. 2018b; Springel et al. 2018; Marinacci et al. 2018) is a state-of-the-art cosmological hydrodynamical simulation that employs a moving-mesh technique based on Voronoi cells, with resolution that adapts to local density. Thanks to its subgrid physics models, the simulation incorporates key physical processes such as star formation, radiative metal cooling, stellar and supermassive black hole feedback, and chemical enrichment from Type II and Type Ia supernovae and AGB stars (for more details, see Pillepich et al. 2018a). To measure the DM, the electron density along the LOS is required. Previous studies (Jaroszyński 2020; Zhang et al. 2021; Takahashi et al. 2021) have already used simulations to create DM maps. In particular, Walker et al. (2024); Zhang et al. (2021); Mo et al. (2022) studied the DM PDF as obtained from IllustrisTNG. However, Konietzka et al. (2025) showed that some of those results suffer from periodic boundary conditions and an insufficient treatment of Voronoi cells. We will therefore use the results from Konietzka et al. (2025) measured at $z = 0.7, 1.5, 3, 4, 5$ as our comparison baseline.

4. RESULTS

In this section, we describe the results of the comparison in detail. To this end, we first compare with the consistency-check simulations in Section 4.1 to provide a consistency check and an estimate for the covariance. We then compare the results to IllustrisTNG in Section 4.2 and demonstrate how the PDF depends on the BFC parameters in Section 4.3. Lastly, we use our results to investigate the assumption of log-normality for the FRB DM PDF in Section 4.4.

4.1. Comparison with the consistency-check simulation

In Figure 3, we present a comparison between the analytical calculation given in Equation (29) and the simulation results. Note that this is the result without clustering, since the consistency simulation randomly places halos. Both methods use the same BFC parameters, with the FRB redshift fixed at $z = 1.5$. The mass range considered spans $10^{10} h^{-1} M_\odot$ to $10^{13} h^{-1} M_\odot$. It is important to note that this result considers only electron density fluctuations, δ_e , and not the mean component. To obtain the observable DM PDF, the mean contribution, which depends solely on cosmological parameters and redshift, must be added to the result. In principle, we would add a two-halo term to the gas profile to make it converge to the cosmic mean on large scales. This, however, is numerically disadvantageous as it leads to a constant in Fourier space and a Dirac delta contribution in DM space, namely the mean. It is therefore much easier to simply calculate the mean and add it later on. This mean is given by the Macquart relation (see e.g. Ioka 2003; Inoue 2004; Deng & Zhang 2014) and can be directly calculated using Equation (2):

$$\langle \text{DM}_{\text{LSS}} \rangle(z) = \frac{3\Omega_b \chi_H}{8\pi G m_p} \chi_e \int_0^z f_{\text{IGM}}(z') \frac{1+z'}{E(z')} dz', \quad (51)$$

with the dimensionless baryon density parameter Ω_b today, the Hubble radius, $\chi_H = c/H_0$, and the electron fraction χ_e given by:

$$\chi_e = Y_H + \frac{1}{2} Y_{\text{He}} \quad (52)$$

$$\approx 1 - \frac{1}{2} Y_{\text{He}}. \quad (53)$$

This is calculated from the primordial hydrogen and helium abundances Y_H and Y_{He} . We assume $Y_H \approx 1 - Y_{\text{He}}$ and $Y_{\text{He}} = 0.245$ (Aver et al. 2015; Planck Collaboration et al. 2020). $f_{\text{IGM}}(z)$ is the gas fraction in the IGM, which can essentially

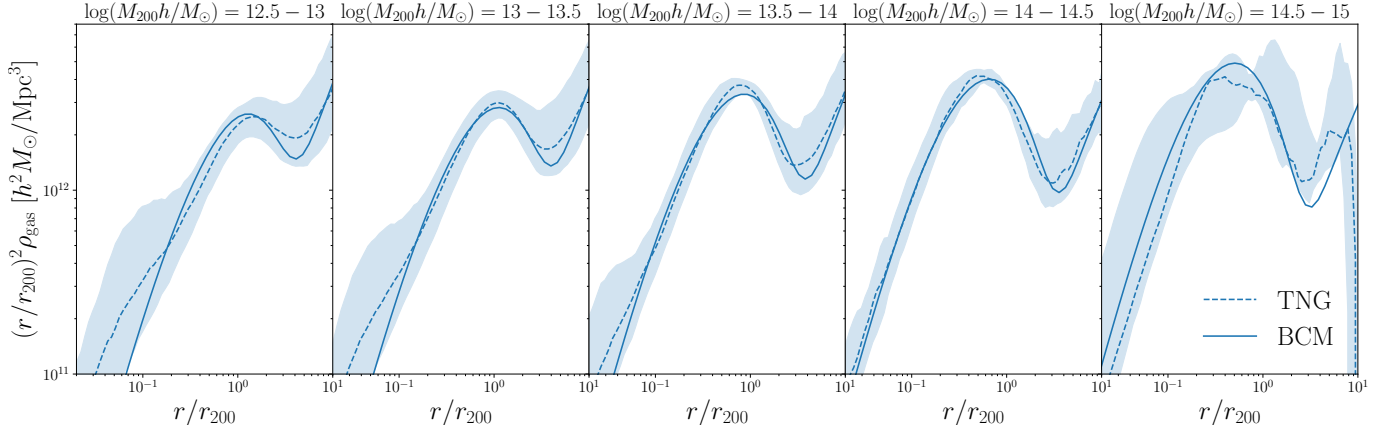


Figure 6.: Comparison of the gas density profiles from the TNG simulation and the BFC model. The solid lines represent the BFC profiles, while the dashed lines show the TNG results. The shaded region indicates the 68% confidence interval of the TNG simulation. All profiles are evaluated in comoving coordinates at redshift 0.5.

be predicted by BFC as the gas fraction:

$$f_{\text{IGM}}(z) = \frac{\int dM f_{\text{hga}}(M, z) M \frac{dn}{dM}(M, z)}{\int dM M \frac{dn}{dM}(M, z)}. \quad (54)$$

The shaded region in Figure 3 represents the 3σ confidence interval computed from the sample covariance. We find good agreement between the simulation and the analytical prediction. The remaining discrepancies can be attributed to two closely related effects. First, both the LOS and halo masses are divided into a finite number of bins, with fixed redshift and mass assigned to all objects within each bin. Increasing the number of bins would improve accuracy and more closely align the simulation with the analytical result.

Second, the dominant contribution to the DM arises from haloes with masses $> 10^{12} h^{-1} M_\odot$. As the number of bins increases, the probability of sampling such massive haloes within a single bin decreases. To ensure adequate statistical sampling of these rare systems, larger bin volumes are required. However, increasing the bin size, which corresponds to larger impact parameters R_{Im} , significantly raises the computational cost of the simulation, especially when running many realisations for the covariance estimation.

We have verified that those two effects indeed explain the remaining discrepancy between the simulation and our analytical results.

4.2. Comparison with IllustrisTNG

To compare the model to the TNG simulation, we first define a likelihood using a covariance matrix. We bin both the TNG PDF and the PDF obtained by the BFC model into $N_{\text{bin}} = 100$ bins and use a covariance matrix obtained by our consistency-check simulation, evaluated at the fiducial parameter values from Table 1 for the BFC. We assume a Gaussian log-likelihood

$$\log(\mathcal{L}) = -\frac{1}{2} \sum_{i,j=0}^{N_{\text{bin}}} \left(p_i^{\text{TNG}} - p_i^{\text{BFC}} \right) \mathbf{C}_{ij}^{-1} \left(p_j^{\text{TNG}} - p_j^{\text{BFC}} \right), \quad (55)$$

where p_i^{TNG} and p_i^{BFC} are the PDF values in bin i^{th} for the TNG and BFC, respectively. Note that the covariance we are using here effectively assumes infinitely many FRBs.

We then sample the likelihood in a Markov Chain Monte Carlo (MCMC) analysis using the ensemble sampler `EMCEE` (Foreman-Mackey et al. 2013). We choose to fit each of the five TNG PDFs at its own redshift. This is due to the fact that the BFC model has mostly been tested and calibrated at redshifts lower than $z = 1.5$, and some model parameters show significant redshift dependence in this regime (see e.g. Schneider et al. 2025). Hence, fitting all redshifts simultaneously could yield erroneous results due to potential redshift-dependent parameter evolution. The prior ranges used for all redshift bins are identical and are listed in Table 1.

The best-fit PDFs derived from the MCMC are shown in Figure 4 alongside their 68 % confidence interval. The results are colour-coded by redshift; the TNG measurements from Konietzka et al. (2025) are shown in dashed, while the best-fit analytical results from BFC are shown as a solid line. As shown, the analytical model agrees well with the hydrodynamical simulation. The corresponding constraints on the parameters of the BFC model are demonstrated in Figure 5. We note again that we performed the fit at each redshift separately, thus allowing us to investigate redshift evolution of the parameters. As can be seen, the primary drivers of the PDF shape are the parameters determining the gas profile, Equation (12). These are M_c , μ and δ . Interestingly, we find that μ depends quite strongly on redshift, preferring a mass-independent slope of the gas profile, β , at higher redshifts since $\mu \rightarrow 0$ leads to a constant β (compare Equation (13)). A large μ will introduce a stronger dependence on M_c . Compared to the parameters obtained in Schneider et al. (2025) for redshifts 0.7 and 1.5, we find that δ is larger and μ is less dependent on redshift. However, one should keep in mind that the redshift range here is much larger. Finally, we note that η and $d\eta$ are not constrained when compared to the prior range in Table 1. These parameters describe the stellar and central galaxy profiles, which are scaled by N_{star} . As the best-fit values obtained for N_{star} are small, the exact shape of the profile is irrelevant, and thus the influence of η or $d\eta$ is negligible. The same is true for the cold gas component, c_{iga} . Comparing the resulting error bars to the constraints of the BFC model obtained by kSZ and X-ray observations (Kovač et al. 2025; Sharma et al. 2025) shows that $\sim 10^4$ FRBs can constrain the BFC parameters to similar precision.

So far, we have only demonstrated that our model is self-

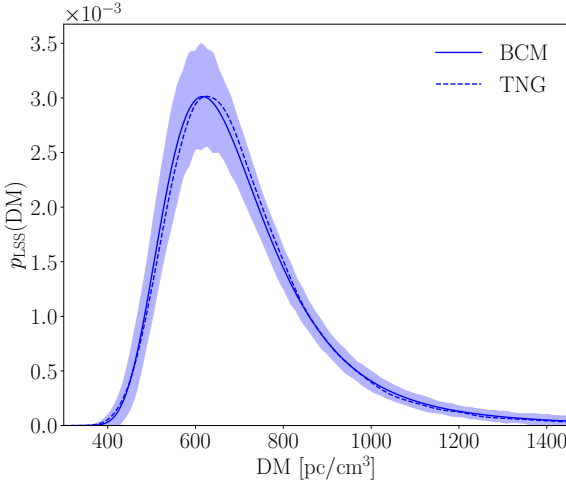


Figure 7. : Comparison between the TNG PDF at redshift 0.7 and the PDF obtained from the BFC model using the best-fit parameters derived from the profiles at the same redshift. The solid line shows the BFC PDF, and the dashed line shows the TNG PDF. The shaded region represents the 3σ confidence interval calculated using the covariance matrix. Note: the solid line is a prediction and not a fit to the dashed line.

consistent and can be fit with eight parameters to a relatively featureless function, i.e., the PDF measured in IllustrisTNG. While we qualitatively compare the derived parameter values with previous work, we now turn the argument around: If we fit the gas profiles in IllustrisTNG with the BFC model, as done in Schneider et al. (2025), can we obtain a consistent prediction for the PDF of the DM? To this end, we re-fit the gas profiles at redshift 0.5 and show the results in Figure 6. As expected, the best-fit BFC profiles describe the IllustrisTNG measurements over a broad mass range reasonably well. We can now use the derived best-fit parameter values and compute the associated DM PDF. The result is shown in Figure 7, and as can be seen, the BFC prediction matches the simulation measurement very well, especially compared to the cosmic variance uncertainty (shaded region). It is important to highlight that the solid line in Figure 7 is not a fit to the dashed line but a prediction. This is a nontrivial result, indicating that BFC provides a self-consistent description of halo gas profiles and integrated quantities, such as the DM PDF. The result is noteworthy for two reasons: (i) the DM is an integrated effect while the profiles are only fitted at a particular redshift, (ii) the DM accumulates contributions from all halo masses, with the weight at a given halo mass given by the number density. Furthermore, previous studies (see e.g. Connor et al. 2025; Medlock et al. 2025; Walker et al. 2024) found that the halo model-based approach for FRBs is difficult, as DM is very sensitive to gas in filaments rather than in halos. Our results demonstrate that this description is indeed possible in a self-consistent manner, at least on the level of the PDF. This is further supported by the fact that halo clustering itself is not particularly important. For other observables, e.g. the power spectrum, the role of filaments might be more important, especially in the transition regime between the one- and two-halo term. This could be alleviated by using a web-based halo model as in Brieden et al. (2025), or by introducing a geometric mean between the one- and two-halo term as for example done in Mead et al. (2015).

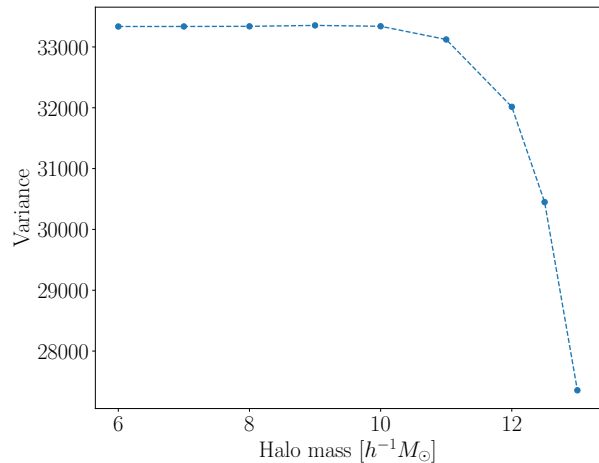


Figure 8. : Dependency of the PDF variance on the lower mass bound at a fixed redshift 0.7.

We investigate this last point in more detail and show how the PDF variance depends on the lower mass bound for all integrals over halo mass in Figure 8. As the lower mass bound decreases, the variance increases, indicating a broader PDF, which is expected. Including low-mass halos in the calculation naturally increases the DM contribution. However, the contribution of an individual low-mass halo is minimal, so we do not expect a drastic impact on the PDF. On the other hand, the halo mass function predicts a large number of low-mass halos, which compensates for their small individual contributions. It is worth noting that, beyond a certain point, further lowering the mass bound does not change the PDF variance. This occurs because halos in that mass regime are too small and have shallow gravitational potentials, allowing feedback processes to expel their gas essentially entirely. With no remaining gas, these halos no longer contribute to the DM. This is, of course, a simplified picture, as very low-mass halos will not host active galactic nuclei and therefore have less feedback. All the relations used in our model are calibrated to halos with masses $M \gtrsim 10^{11} h^{-1} M_\odot$. One might therefore raise the suspicion that the plateau at low masses seen in Figure 8 is somewhat an artefact of the BFC rather than a genuine physical feature. However, we tested what happens if halos retain an unrealistic amount of gas at low masses, in particular, a mass-independent gas fraction $f_{\text{hga}} = f_b$. Even in this case, variance saturates at $10^8 h^{-1} M_\odot$ and only changes by around 5 % relative to $10^{10} h^{-1} M_\odot$. Therefore, even if halos at lower masses would retain their gas, the result would not change much, as the higher abundance of low-mass halos can not compensate for the drop in the gas density at some point. This finding is in line with Figure 1 in Sharma et al. (2025). Throughout this paper, we therefore restrict our analysis to halos in the mass range $10^{10} h^{-1} M_\odot$ to $10^{16} h^{-1} M_\odot$.

4.3. Effect of the BFC Parameters

One of the main benefits of BFC is that one can study how different observables (here, the DM PDF) depend on physically motivated feedback parameters and, hence, on the underlying density profiles. This is almost impossible in hydrodynamical simulations. If one, for example, can identify parameters which are irrelevant for cosmological studies, the complexity of the BFC model can be reduced. In this section,

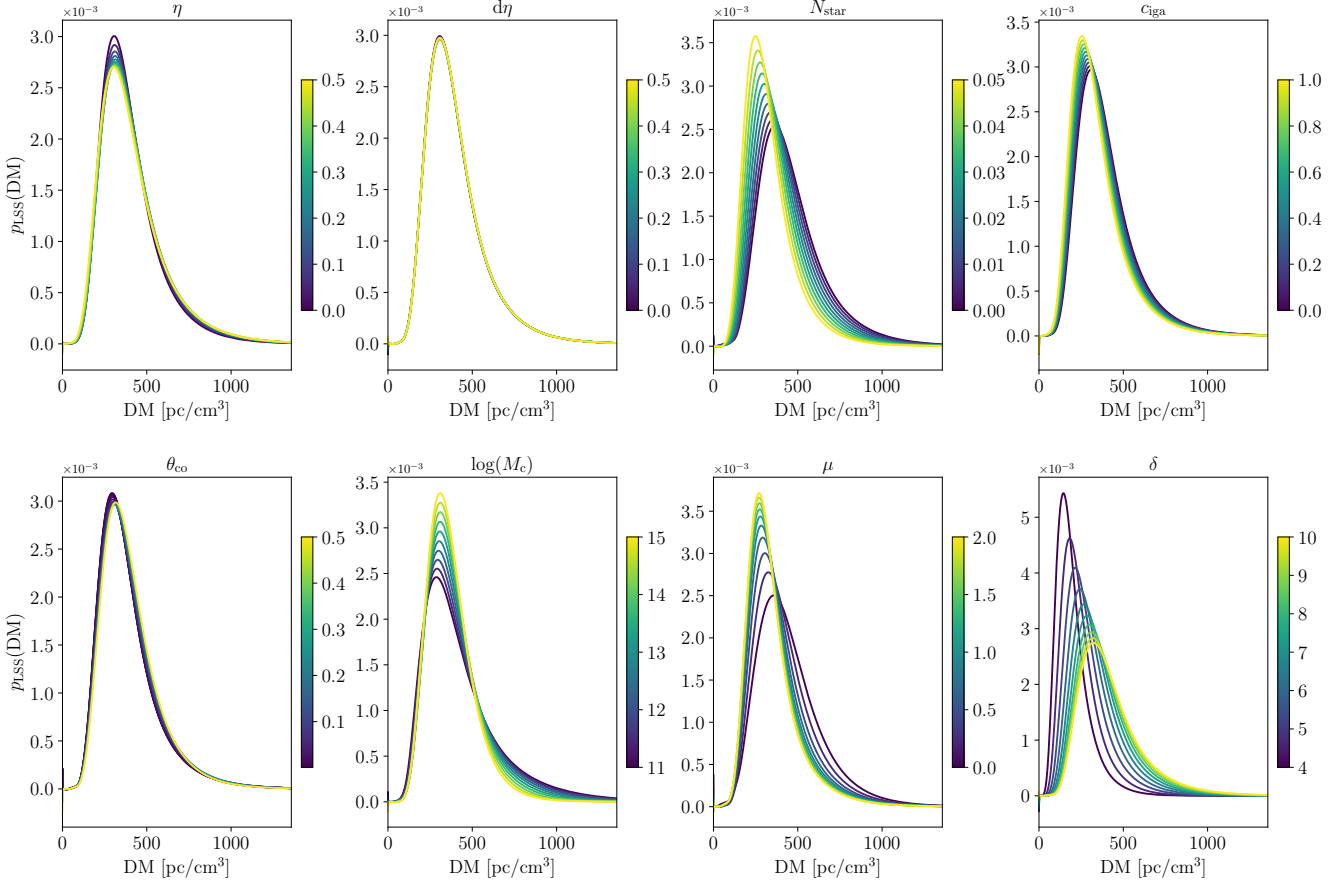


Figure 9. : Impact of varying individual BFC parameters on the predicted DM PDF at redshift 0.7. In each panel, only one parameter is varied at a time, with values indicated in the colourbar. All the others are held at their fiducial values shown in Table 1. Parameters with a direct influence on the gas distribution, such as M_c , μ , and δ , produce more significant changes in the shape of the PDF.

we therefore examine how the DM PDF depends on various BFC parameters.

To isolate the effect of each parameter, we fix all others to their fiducial values (i.e., the best-fit parameter for TNG as shown in Table 1) and vary only one at a time. Note that we do not fix the mean of the corresponding distributions. The results are shown in Figure 9, and the observed trends are consistent with the MCMC results presented in Figure 5.

In BCM, there are three parameters, M_c , μ , and δ , that directly influence the gas profile, and as can be seen from Figure 9, these have the largest effect on the DM PDF. Increasing parameters such as M_c and μ makes the gas profile shallower, indicating that less gas remains concentrated within the halo, i.e. stronger feedback. This corresponds to a more homogeneous distribution of gas, which reduces the variation in DM along different lines of sight at a fixed redshift, making the PDF more sharply peaked. This can be compared to the limiting case of a perfectly homogeneous gas distribution, which results in a Dirac delta PDF equal to the mean. The parameter δ , however, has the opposite effect: increasing it makes the gas more concentrated inside the halo, resulting in a broader PDF.

On the other hand, parameters such as η and $d\eta$, which influence the stellar contribution, have only a small effect on the PDF. The reason is that they solely influence the stellar mass fraction as a function of halo mass, which in turn is scaled

by N_{star} . So these parameters induce a secondary effect on the stellar profile, which only indirectly changes the gas profile via Equation (12). Generally, if $\eta + d\eta$ is larger, the stellar fraction decreases more rapidly with halo mass, leading to a larger gas fraction and, consequently, a slightly broader PDF. This can be seen as follows: if the gas fraction is multiplied by some factor f , the random variable DM is simply rescaled $\text{DM} \rightarrow f\text{DM}$, as are the corresponding moments. Thus, if this factor is larger than unity, the PDF becomes broader. For N_{star} , this influence is more direct: an increase leads to less gas in the halos because it is locked up in stars and hence to a narrower PDF, again by rescaling the random variable DM. Adding more cold gas by increasing c_{iga} has the same effect. We also see relatively little influence of θ_{co} as only those sightlines that pass through the halo centre are sensitive to this parameter. However, if feedback is weak overall, the gas is more centrally concentrated, and therefore significant contributions to the DM occur only close to the halo centre. Hence, one can expect the PDF to be more sensitive to θ_{co} if feedback is weak.

4.4. The case of the log-normal distribution

In this section, we test whether the DM PDF measured from IllustrisTNG can be well-described by a log-normal distribution. Konietzka et al. (2025) indicated that, at low redshift, the PDF is not best described by a log-normal distribution.

For this purpose, we take the results of the TNG simulation at redshift $z = 0.7$ as our reference dataset and fit it with a log-normal (compare to Figure 13 in Konietzka et al. 2025). Alternatively, we could fit the log-normal variance of the corresponding PDF directly to the BFC parameters. However, we are mainly interested in the goodness-of-fit for the log-normal as it is commonly used in FRB analyses. The question we hence want to answer is: how many FRBs are required to distinguish the log-normal fit from the real (IllustrisTNG) distribution?

To this end, we perform a χ^2 test. We again assume a Gaussian likelihood, Equation (55), where p_i^{BFC} is now replaced by p_i^{LN} . To compute the covariance matrix, following the procedure in the previous section, we first divide the PDF into 100 bins and then run multiple realisations of our consistency simulations to estimate the cosmic-variance contribution as before. To account for the finite number of FRBs, we add noise to each bin by drawing a random number from a normal distribution with zero mean and variance:

$$\sigma_{\text{noise}}^2 = \frac{p_i}{N_{\text{FRB}} \Delta \text{DM}_i}, \quad (56)$$

where p_i is the PDF value in the i -th bin and ΔDM_i is the corresponding DM width. This approach effectively models the increased uncertainty at low FRB counts: for small N_{FRB} , the fluctuations are large, while at the limit $N_{\text{FRB}} \rightarrow \infty$ this contribution to the uncertainty vanishes. In principle, this effect is included in our simulation. However, we choose to estimate the covariance from many sightlines $N_{\text{FRB}} \rightarrow \infty$ and add this contribution by hand. From the Gaussian statistic, we can immediately estimate the χ^2 and hence the p -value given the degrees of freedom.

The previous approach is only valid under the assumption of a Gaussian likelihood, which does not hold in our case. For consistency, we also adopt the following procedure. We begin by drawing N_{FRB} samples from the TNG simulation. We then approximate these sampled values with a log-normal distribution by maximising the likelihood of the data. In practice, this is done by estimating the parameters of the log-normal PDF, p^{LN} , that maximise

$$\log(\mathcal{L}) = \sum_{i=1}^{N_{\text{FRB}}} \log [p^{\text{LN}}(\text{DM}_i)] \quad (57)$$

where DM_i are the dispersion measures drawn from the TNG simulation.

We estimate the p -value as follows: we generated N random realisations from the likelihood evaluated at the maximum posterior. These realisations serve as an alternative to the usual χ^2 statistics. By comparing the log-likelihood of the actual data, χ^2_{data} , with those of the simulated realisations, we can estimate the one-sided p -value (or probability-to-exceed) as

$$p_{\text{te}} = P(\chi_i^2 > \chi_{\text{data}}^2). \quad (58)$$

Figure 10 shows how the $\Delta\chi^2$ (solid blue curve) for the Gaussian likelihood and the corresponding p -values (blue dashed) as a function of N_{FRB} . For the latter, we assume that we fit only a single parameter, i.e., the amplitude of the DM-redshift relation. The corresponding version of the exact likelihood, i.e. Equations (57) and (58), is shown as the red dashed line. The noise occurs because of the random draws of the data. One can, however, see that the overall behaviour is the same and

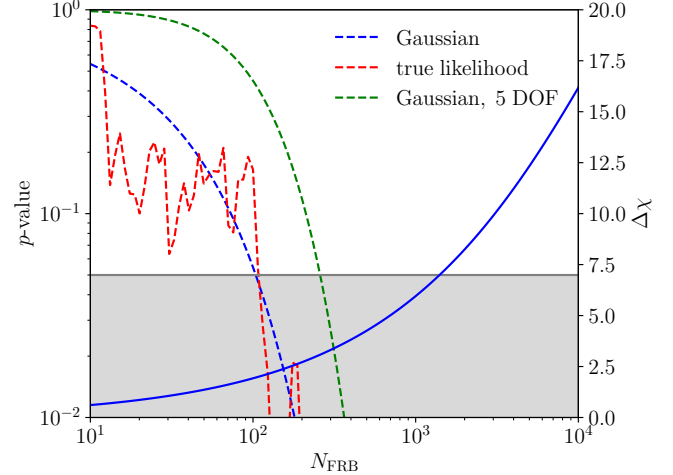


Figure 10. : Goodness-of-fit as a function of FRBs observed, N_{FRB} . The dashed curves show the p -values. Blue and green show the p -value obtained from the Gaussian likelihood assumption, Equation (55), for one and five degrees of freedom (DOF), respectively. In red we show $1 - p_{\text{te}}$, Equation (58), thus dropping the Gaussian likelihood assumption. The solid curve indicates the corresponding $\Delta\chi^2$ for the Gaussian case. We show the typical p -value threshold of $p = 5 \times 10^{-2}$ as the grey shaded area.

that the p -value drops below the commonly accepted value of 5×10^{-2} at around 10^2 FRBs (as indicated by the grey-shaded area). If we assume that a typical analysis uses at least five free parameters¹, we can see from Figure 10 that the p -value drops below 5×10^{-2} for a few hundred FRBs. Hence, using the log-normal approximation for the PDF is sufficient unless more than a few hundred FRBs are being analysed. Coincidentally, this is also the number of FRBs at which correlations between the different sightlines will bias parameter estimation as well (Reischke & Hagstotz 2023b).

5. SUMMARY & CONCLUSION

In this work, we present a fast, fully analytical framework for predicting the one-point PDF of the DM for FRBs using a baryonification (BFC) model. The theoretical modelling was tested and validated against consistency simulations and full hydrodynamical simulations using IllustrisTNG. Our model provides an efficient alternative to expensive hydrodynamical simulations for studying FRBs in a cosmological setting. To accelerate subsequent calculations, we used COSMOPOWER to train a machine learning emulator that enables rapid evaluations across parameter space without recalculating the full analytical expression for each parameter set. The principal results of the paper can be summarised as follows:

- i) The model reproduces the IllustrisTNG simulation at five different redshifts ($z = 0.7, 1.5, 3, 4$, and 5), finding excellent agreement between the analytical predictions and the hydrodynamical simulation results.
- ii) We demonstrated the self-consistency of our approach by fitting gas density profiles from the TNG simulation

¹ This could be a couple of cosmological parameters and two parameters for the host contribution.

with the BFC model and subsequently using the best-fit parameters to predict the DM PDF and vice versa. This confirms that the BFC model produces physically consistent descriptions of both local gas distributions and integrated statistics such as the DM PDF.

- iii) We identified the BFC parameters that determine the PDF shape: the pivot mass scale M_c , the mass-dependent slope parameter μ , and the outer transition parameter δ . These parameters, which directly control the gas profile, emerged as the primary drivers of the PDF morphology, whereas parameters describing the stellar and cold gas components had only minor effects. A survey with $\sim 10^4$ FRBs can constrain the gas parameters of the BFC model to similar precision as kSZ and X-ray observations (see as well [Kovač et al. 2025](#); [Sharma et al. 2025](#)). Therefore, FRBs provide an independent measurement of the gas distribution, sensitive to different halo masses and systematics.
- iv) We used our pipeline to determine how well the FRB DM PDF can be described by a log-normal distribution, and for which number of FRBs this approximation breaks down ([Konietzka et al. 2025](#)). We demonstrated that while this simple functional form provides an adequate description for a few hundred FRBs, the approximation becomes distinguishable from the true PDF for larger samples.

We want to highlight that gas density profiles fit to hydrodynamical simulations can accurately predict the PDF of the DM without fitting the PDF itself, providing a non-trivial validation of the halo model approach for FRBs. This result suggests that FRBs, despite their sensitivity to gas distributed throughout the circumgalactic and intergalactic media rather than just within virialised halos, can still be modelled within a halo-centric framework when considering integrated quantities. This opens the door for consistent multi-observable constraints on baryonic physics, including FRBs.

ACKNOWLEDGEMENTS

We would like to thank Zheng Zhang for many helpful conversations about emulators and MomentEMU. AN acknowledges support from the European Research Council (ERC) under the European Union’s Horizon 2020 research and innovation program with Grant agreement No. 101163128, as well as from the University of Manchester. SKG acknowledges the support by NWO (grant no OCENW.M.22.307) and Olle Engkvist Stiftelse (grant no. 232-0238). SH was supported by the Excellence Cluster ORIGINS which is funded by the Deutsche Forschungsgemeinschaft (DFG, German Research Foundation) under Germany’s Excellence Strategy - EXC-2094 - 390783311. We used `matplotlib` ([Hunter 2007](#)) for plots. A lot of the computations were done with the help of `SciPy` ([Virtanen et al. 2020](#)) and `NumPy` ([Harris et al. 2020](#)).

REFERENCES

Anbajagane D., Pandey S., Chang C., 2024, [OJA](#), **7**, 108
 Andersen B., et al., 2020, [Nat.](#), **587**, 54
 Aricò G., Angulo R. E., Hernández-Monteagudo C., Contreras S., Zennaro M., 2021a, [MNRAS](#), **503**, 3596
 Aricò G., Angulo R. E., Contreras S., Ondaro-Mallea L., Pellejero-Ibañez M., Zennaro M., 2021b, [MNRAS](#), **506**, 4070
 Astropy Collaboration et al., 2022, [ApJ](#), **935**, 167
 Aver E., Olive K. A., Skillman E. D., 2015, [JCAP](#), **2015**, 011
 Baltz E. A., Marshall P., Oguri M., 2009, [JCAP](#), **1**, 15
 Brieden S., Beutler F., Pellejero-Ibañez M., 2025, [arXiv e-prints](#), p. [arXiv:2508.10902](#)
 Burger P. A., et al., 2025, [arXiv e-prints](#), p. [arXiv:2506.18974](#)
 Champion D. J., et al., 2016, [MNRAS](#), **460**, L30
 Chatterjee S., et al., 2017, [Nat.](#), **541**, 58
 Chisari N. E., et al., 2019a, [OJA](#), **2**, 4
 Chisari N. E., et al., 2019b, [APJ Supplement Series](#), **242**, 2
 Collaboration E., Mellier Y., et al., 2025, [A&A](#), **697**, A1
 Connor L., Sievers J., Pen U.-L., 2016, [MNRAS](#), **458**, L19
 Connor L., et al., 2025, [Nat. Astr.](#),
 Cordes J. M., Lazio T. J. W., 2002, [arXiv e-prints](#), pp [astro-ph/0207156](#)
 Deng W., Zhang B., 2014, [ApJ](#), **783**, L35
 Fluri J., Kacprzak T., Lucchi A., Schneider A., Refregier A., Hofmann T., 2022, [Phys. Rev. D](#), **105**, 083518
 Foreman-Mackey D., Hogg D. W., Lang D., Goodman J., 2013, [PASP](#), **125**, 306
 Giri S. K., Schneider A., 2021, [JCAP](#), **2021**, 046
 Grandis S., Aricò G., Schneider A., Linke L., 2024, [MNRAS](#), **528**, 4379
 Hagstotz S., Reischke R., Lilow R., 2022, [MNRAS](#), **511**, 662
 Harris C. R., et al., 2020, [Nat.](#), **585**, 357
 Hunter J. D., 2007, [CiSE](#), **9**, 90
 Inoue S., 2004, [MNRAS](#), **348**, 999
 Ioka K., 2003, [ApJ](#), **598**, L79
 James C. W., et al., 2022, [MNRAS](#), **516**, 4862
 Jaroszyński M., 2020, [AcA](#), **70**, 87
 Konietzka R. M., Connor L., Semenov V. A., Beane A., Springel V., Hernquist L., 2025, [arXiv e-prints](#), p. [arXiv:2507.07090](#)
 Kovač M., et al., 2025, [JCAP](#), **2025**, 046
 LSST Science Collaboration et al., 2009, preprint, 0912, [arXiv:0912.0201](#)
 Lee M. E., Lu T., Haiman Z., Liu J., Osato K., 2023, [MNRAS](#), **527**, 1124
 Lewis A., Challinor A., Lasenby A., 2000, [ApJ](#), **538**, 473
 Lorimer D. R., Bailes M., McLaughlin M. A., Narkevic D. J., Crawford F., 2007, [Sci.](#), **318**, 777
 Macquart J.-P., et al., 2020, [Nat.](#), **581**, 391
 Marinacci F., et al., 2018, [MNRAS](#), **480**, 5113
 McCarthy I. G., Schaye J., Bird S., Le Brun A. M. C., 2017, [MNRAS](#), **465**, 2936
 McQuinn M., 2014, [ApJL](#), **780**, L33
 Mead A. J., Peacock J. A., Heymans C., Joudaki S., Heavens A. F., 2015, [MNRAS](#), **454**, 1958
 Mead A. J., Tröster T., Heymans C., Van Waerbeke L., McCarthy I. G., 2020, [A&A](#), **641**, A130
 Medlock I., Nagai D., Singh P., Oppenheimer B., Anglés-Alcázar D., Villaescusa-Navarro F., 2024, [ApJ](#), **967**, 32
 Medlock I., Nagai D., Anglés-Alcázar D., Gebhardt M., 2025, [ApJ](#), **983**, 46
 Mo J.-F., Zhu W., Wang Y., Tang L., Feng L.-L., 2022, [MNRAS](#), **518**, 539
 Navarro J. F., Frenk C. S., White S. D. M., 1997, [ApJ](#), **490**, 493
 Nelson D., et al., 2019, [CompAC](#), **6**, 2
 Ocker S. K., Cordes J. M., 2024, [RNAAS](#), **8**, 17
 Ocker S. K., Cordes J. M., Chatterjee S., 2020, [ApJ](#), **897**, 124
 Osato K., Nagai D., 2023, [MNRAS](#), **519**, 2069
 Petroff E., et al., 2015, [MNRAS](#), **447**, 246
 Pillepich A., et al., 2018a, [MNRAS](#), **473**, 4077
 Pillepich A., et al., 2018b, [MNRAS](#), **475**, 648
 Planck Collaboration et al., 2016, [A&A](#), **594**, A13
 Planck Collaboration et al., 2020, [A&A](#), **641**, A6
 Reischke R., Hagstotz S., 2023a, [MNRAS](#), **523**, 6264
 Reischke R., Hagstotz S., 2023b, [MNRAS](#), **524**, 2237
 Reischke R., Hagstotz S., 2025, [arXiv e-prints](#), p. [arXiv:2507.17742](#)
 Reischke R., Kovač M., Nicola A., Hagstotz S., Schneider A., 2025, [OJA](#), **8**, 127
 Schneider A., Teyssier R., 2015, [JCAP](#), **12**, 049
 Schneider A., Teyssier R., Stadel J., Chisari N. E., Le Brun A. M. C., Amara A., Refregier A., 2019, [JCAP](#), **2019**, 020
 Schneider A., et al., 2020, [JCAP](#), **04**, 020
 Schneider A., Giri S. K., Amodeo S., Refregier A., 2022, [MNRAS](#), **514**, 3802
 Schneider A., et al., 2025, [JCAP](#), **2025**, 043
 Sharma K., Krause E., Ravi V., Reischke R., R. S. P., Connor L., 2025, [ApJ](#), **989**, 81
 Springel V., et al., 2018, [MNRAS](#), **475**, 676
 Spurio Mancini A., Piras D., Alsing J., Joachimi B., Hobson M. P., 2022, [MNRAS](#), **511**, 1771
 Takahashi R., Ioka K., Mori A., Funahashi K., 2021, [MNRAS](#), **502**, 2615

Theis A., Hagstotz S., Reischke R., Weller J., 2024, arXiv e-prints, p. arXiv:2403.08611

Thiele L., Hill J. C., Smith K. M., 2019, Phys. Rev. D, 99, 103511

Thornton D., et al., 2013, Science, 341, 53

Tinker J., Kravtsov A. V., Klypin A., Abazajian K., Warren M., Yepes G., Gottlöber S., Holz D. E., 2008, ApJ, 688, 709

Tröster T., et al., 2022, A&A, 660, A27

Virtanen P., et al., 2020, Nat. Methods, 17, 261

Walker C. R. H., Spitler L. G., Ma Y.-Z., Cheng C., Artale M. C., Hummels C. B., 2024, A&A, 683, A71

Yao J. M., Manchester R. N., Wang N., 2017, ApJ, 835, 29

Zhang Z. J., Yan K., Li C. M., Zhang G. Q., Wang F. Y., 2021, ApJ, 906, 49

Zhou A. J., Gatti M., Anbajagane D., Dodelson S., Schaller M., Schaye J., 2025, JCAP, 2025, 073

Zürcher D., Fluri J., Ajani V., Fischbacher S., Refregier A., Kacprzak T., 2023, MNRAS, 524, 5212

APPENDIX

A. COSMOPOWER

To generate the training data set, we calculated 110,000 PDFs that cover a wide range of parameter values. The parameter ranges used to generate this data are the same as the prior ranges listed in Table 1, apart from $\delta \in [1, 11]$. After training, we validate the emulator using a separate test data set. Although the test parameters are within the same ranges as the training data set (as given in Table 1), they are sampled independently and are not part of the training data set. For the `cosmopower`, we use `cosmopower_PCAplusNN`, i.e. a principal component analysis compression before training the neural network. Four hidden layers, each with 512 nodes, are used, and the neural network is trained in 6 learning steps with a batch size of 1024.

Figure A.1 illustrates the accuracy of the emulator. The x-axis represents the value of DM normalised by its mean at a given redshift, while the y-axis shows the relative difference between the emulated and true DM values, normalised by the minimum of their respective peaks. The plot demonstrates that 99% of the test dataset exhibits a relative difference of less than 0.004. This result validates the emulator's performance.

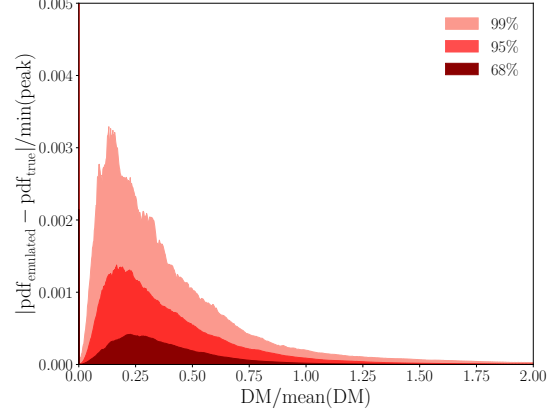


Figure A.1.: Accuracy of the emulator evaluated over the test data set. The plot shows the distribution of the relative difference between the emulated and true DM, normalised by the minimum of the two peaks. The shaded regions indicate that 68%, 95%, and 99% of the test samples have relative differences below 0.001, 0.002, and 0.004, respectively, demonstrating high emulator precision.

This paper was built using the Open Journal of Astrophysics L^AT_EX template. The OJA is a journal which provides peer review for new papers in the `astro-ph` section of the arXiv. Learn more at <http://astro.theoj.org>.